Research Square

Preprints are preliminary reports that have not undergone peer review.
They should not be considered conclusive, used to inform clinical practice,
or referenced by the media as validated information.

Energy-Level-Guided Selection ofHole-Collecting Monolayers for p-i-n Perovskite Solar Cells

Aruto Akatsuka
Chiba University
Koki Sawai
Chiba University
Hiroyuki Yoshida
hyoshida@chiba-u.jp

Chiba University

Article

Keywords:

Posted Date: November 20th, 2026

DOI: https://doi.org/10.21203/rs.3.rs-11514214/v1

License: This work is licensed under a Creative Commons Attribution 4.0 International License.
Read Full License

Additional Declarations: No competing interests reported.

Energy-Level-Guided Selection of Hole-Collecting Monolayers for p-i-n Perovskite Solar Cells

Aruto Akatsuka[1], Koki Sawai[1], and Hiroyuki Yoshida[*1,2]

1. Graduate School of Engineering, Chiba University, 1-33 Yayoi-cho, Inage-ku, Chiba, Japan
2. Molecular Chirality Research Center, Chiba University, 1-33 Yayoi-cho, Inage-ku, Chiba, Japan

E-mail: hyoshida@chiba-u.jp

* Corresponding author

Abstract

Harnessing solar energy is crucial for reducing greenhouse gas emissions and mitigating climate change. Among emerging photovoltaic technologies, metal halide perovskite solar cells (PSCs) have attracted considerable attention owing to their high power conversion efficiencies (PCEs) and low manufacturing costs. In particular, inverted-architecture (p-i-n) PSCs incorporating hole-collecting monolayers (HCMs) have emerged as promising alternatives to conventional (n-i-p) PSCs employing Spiro-OMeTAD-based hole-transport layers, which can suffer from stability issues. These inverted PSCs have improved operational stability and PCEs. A wide variety of HCMs have been developed, but their hole-collection efficiencies depend strongly on the combination of HCM and perovskite materials. Therefore, selecting an appropriate HCM for a given perovskite is essential for achieving high efficiency PSCs. Here, we establish a practical guideline for selecting HCMs based on energy level alignment. We focus on five representative carbazole-based HCMs: 2PACz, MeO-2PACz, Me-2PACz, Me-4PACz, and 3PATAT-C3. By combining experimentally determined energy parameters of these HCMs with the universal energy level alignment model proposed in our previous work, we evaluated the compatibility of these HCMs with given perovskites. We then tested the proposed guideline by examining the correlation between the model-predicted hole-collection efficiencies and previously reported photovoltaic performance. This framework enables rational selection of HCMs for diverse perovskites, thereby minimizing trial-and-error screening in the development of high-efficiency PSCs.

Keywords: Perovskite solar cells; Hole-collecting monolayers; Energy level alignment; Work function; Ionization energy

1. Introduction

The development of efficient and sustainable photovoltaic devices is essential for achieving carbon-neutral energy systems. Metal halide perovskite solar cells (PSCs) have emerged as promising next-generation photovoltaic devices because they combine high power conversion efficiencies (PCEs) achieving 28%[1], with low-cost, energy-efficient manufacturing through low-temperature solution processing[2,3]. Metal halide perovskites possess distinctive optoelectronic properties, including strong light absorption[4], long carrier diffusion lengths[5], low trap-state densities[6], and tunable bandgaps[7,8]. These characteristics enable efficient charge generation and transport in polycrystalline thin films[9,10] and have driven rapid improvements in PCE.

PSCs can be classified into two main device architectures: regular (n-i-p) and inverted (p-i-n) configurations. In these configurations, electron-collecting and hole-collecting layers are deposited on the transparent electrode, respectively. n-i-p PSCs have historically exhibited higher PCEs than inverted PSCs[11]. However, conventional hole-collecting materials such as Spiro-OMeTAD often require dopants, which can adversely affect long-term device stability[12]. In contrast, p-i-n PSCs can employ dopant-free hole-collecting materials while achieving high PCEs and improved device stability[11]. In recent years, hole-collecting monolayers (HCMs) have gained widespread use as alternatives to conventional polymer materials such as poly(3,4-ethylenedioxythiophene)-poly(styrenesulfonate) (PEDOT:PSS) and poly[bis(4-phenyl)(2,4,6-trimethylphenyl)amine] (PTAA)[11]. HCMs are ultrathin and strongly adsorbed onto transparent electrodes, reducing parasitic light absorption and hole-transport loss while improving device stability[13,14]. To enhance PCE and operational stability through interface modification, many HCM molecules have been developed with an emphasis on increasing orbital overlap with the perovskite[15], improving conductivity[16], passivating defects[17], promoting uniform film formation[18], and increasing the built-in potential[19,20].

While these molecular design strategies have attracted attention, appropriate energy level alignment with the perovskite is a more fundamental prerequisite for HCMs to efficiently collect holes[21]. Such energy

level alignment has often been described using either the vacuum-level alignment model[22,19] or the Schottky-junction model[23–25]. The vacuum-level alignment model assumes that the energy levels of the HCM and perovskite are aligned with respect to the vacuum level; hole-collection efficiency is then evaluated from the difference between their ionization energies (IEs), ΔIE. In contrast, the Schottky-junction model assumes Fermi-level alignment between the HCM-modified transparent electrode and the perovskite. The hole collection is evaluated in terms of band bending in the perovskite, as determined by the work-function difference, ΔWF. However, both models have limitations. The former neglects the interface dipole and the band bending in the perovskite layer, whereas the latter does not account for hole transport through the highest occupied molecular orbital (HOMO) level of the HCMs. As a result, the energy level alignments predicted by these models do not always correlate with the experimentally observed hole-collection efficiency.

To address these limitations, we previously proposed a universal energy level alignment model for transparent electrode/HCM/perovskite interfaces[21]. In this model, the hole-collection efficiencies are governed by both the energy barrier at the HCM/perovskite interface and band bending in the perovskite layer. The model successfully reproduced the differences in hole-collection efficiency among HCMs with diverse molecular structures, demonstrating its applicability across a wide range of HCMs.

However, our previous assessment focused primarily on the model's applicability across different HCM molecular structures, whereas its applicability to different perovskites remains largely unexplored. Perovskites with diverse compositions and energy levels have been developed for different applications. For example, narrow-bandgap perovskites are usually used for single-junction and semitransparent PSCs[26,27]. In all perovskite tandem solar cells, bandgap optimization is essential for both the narrow-bandgap bottom cell and the wide-bandgap top cell[28,29]. Such bandgap tuning is typically achieved by adjusting the iodide-to-bromide or chloride ratio and by partially or completely replacing lead with tin. These compositional changes alter not only the optical bandgap but also the IE, electron affinity (EA), and work function (WF)[8]. Therefore, selecting an appropriate HCM for a given perovskite is critical,

highlighting the need for a straightforward and easily applicable guideline for HCM selection.

In this work, we apply our universal energy level alignment model to demonstrate the suitable HCM selection for perovskites with different energy levels. We examine five representative carbazole-based HCMs with different energy parameters: [4-(3,6-dimethyl-9H-carbazol-9-yl)butyl]phosphonic acid (Me-4PACz), [2-(3,6-dimethyl-9H-carbazol-9-yl)ethyl]phosphonic acid (Me-2PACz)[30]. [2-(9H-carbazol-9-yl)ethyl]phosphonic acid (2PACz), [2-(3,6-dimethoxy-9H-carbazol-9-yl)ethyl]phosphonic acid (MeO-2PACz)[22], and [[5H-diindolo[3,2-a:3′,2′-c]carbazole-5,10,15-triyl]tris(propane-3,1-diyl)]tris(phosphonic acid) (3PATAT-C3)[15]. We first determined the precise energy parameters of Me-2PACz and Me-4PACz using ultraviolet photoelectron spectroscopy (UPS) and low energy inverse photoelectron spectroscopy (LEIPS)[31–33]; parameters for the remaining HCMs are taken from our previous work[21]. In our previous work, we found that HCM molecules form an interface dipole on transparent electrodes, modulating their WF[21]. Here, we further investigated the relationship between molecular orientation and the magnitude of this interface dipole using UPS and metastable atom electron spectroscopy (MAES)[34]. We then selected suitable HCMs for various perovskites focusing on solar cell applications, single-, double-, and triple-cation perovskites with different iodide-to-bromide (I/Br) ratios. The energy parameters of the perovskites are taken from the literature[8,35–37] and our previous work[21]. This work aims to establish a practical framework for selecting suitable HCMs for a wide range of perovskites.

2. Results and discussion

2.1. Experimental determination of energy parameters

Figures 1a and 1b show the UPS and LEIPS results for Me-2PACz/ITO, Me-4PACz/ITO, and pristine ITO. The WFs were derived from the secondary electron cutoff in the UPS spectra (Figure 1a). The WF of pristine ITO (WF_{ITO}) was 4.23 eV and increased by approximately 0.2 eV upon deposition of either molecule. The WF of Me-2PACz/ITO was almost the same as that of Me-4PACz/ITO. Figure 1b shows the UPS and LEIPS spectra near the Fermi level. The IE of Me-2PACz was 5.54 eV, slightly lower than that of Me-4PACz (5.66 eV). The EAs of Me-2PACz and Me-4PACz were identical at 1.57 eV.

Figure 1c summarizes the WF shifts of Me-2PACz and Me-4PACz with respect to WF_{ITO} and their IEs and EAs, with the previously reported values for 2PACz, MeO-2PACz, and 3PATAT-C3[21]. In this section, we compare the WF shift which is the WF of HCM-modified ITO (WF_{HCM}) with respect to that of the ITO substrate, WF_{ITO}. In our previous work, we found that WF_{HCM} depends on WF_{ITO}, whereas the HCM-induced WF shift is an intrinsic property of the HCM that reflects the interface dipole generated by the HCM[21]. As shown in Figure 1c, the magnitude of the interface dipole increased in the order MeO-2PACz < 3PATAT-C3 < Me-2PACz ≒ Me-4PACz < 2PACz, with 2PACz showing the largest value of 0.47 eV. For the energy level alignments discussed below, we calculated WF_{HCM} by adding the magnitude of the interface dipole to a reference WF_{ITO} of 4.75 eV for UV–ozone-treated ITO. The WF_{ITO} can vary in the range from 4.2 to 4.85 eV depending on the surface cleanliness and treatment method[38,39].

The IEs and EAs of the HCMs (IE_{HCM} and EA_{HCM}) ranged from 5.21 to 5.84 eV and from 1.48 to 1.90 eV, respectively. In particular, their EA_{HCM}s were 1.43–2.57 eV lower than those of the perovskites[40], suggesting effective electron-blocking properties to reduce the open circuit voltage (V_{OC}) loss[41]. The Fermi levels of all molecules lay 0.4–0.66 eV above the HOMO level, indicating that all the molecules exhibit p-type semiconductor behavior.

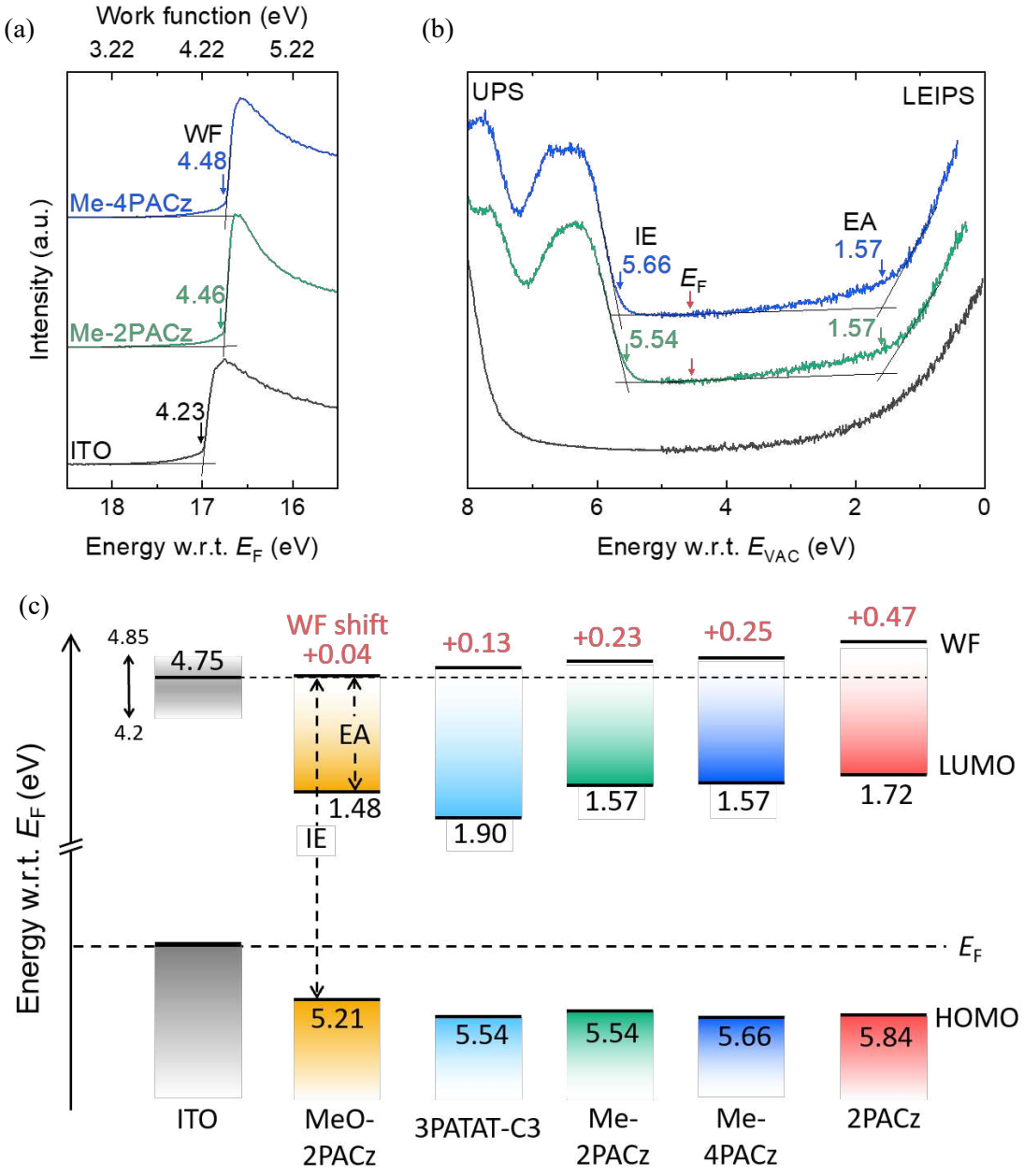


Figure1 Experimental determination of energy parameters of hole-collecting monolayers. (a) Secondary electron cutoff region of the UPS spectra used to determine WF_{ITO} and WF_{HCM}. (b) UPS and LEIPS spectra around the Fermi level (the energy with reference to the vacuum level), the onset of which corresponds to the IE and the EA. (c) Energy-level diagram showing the work-function shifts induced by the interfacial dipoles, ionization energies (IEs), and electron affinities (EAs) of the HCMs. The values for Me-2PACz and Me-4PACz were determined in this study, whereas those for the other HCMs were taken from our previous work (Ref. 21).

2.2. Determination of molecular orientation

To elucidate the magnitude of the interface dipole created by HCMs, we investigated the molecular orientations of the HCMs. Based on the Helmholtz equation (Eq.1), the magnitude of the interface dipole is expressed in terms of the molecular dipole moment perpendicular to the surface, $\mu_{\perp}$. This perpendicular component is given by $\mu_{\perp} = \mu\cos\theta$, where μ is the molecular dipole moment and θ is its angle relative to the surface normal. The magnitude of the interface dipole is expressed as,

$$\frac{e\mu_{\perp}}{\varepsilon_0\varepsilon_{\mathrm{eff}}}\frac{N}{A} = \frac{e\mu\cos\theta}{\varepsilon_0\varepsilon_{\mathrm{eff}}}\frac{N}{A} \quad \text{(Eq.1)}$$

where e is the elementary charge, ε_0 is the vacuum permittivity, $\varepsilon_{\mathrm{eff}}$ is the effective permittivity, N is the number of adsorbed molecules, and A is the surface area; N/A represents the molecular surface density. Therefore, the molecular orientation on ITO is required to calculate this equation. However, determining molecular orientation on ITO and FTO is challenging, because their surface roughness limits the applicability of standard techniques such as variable-angle spectroscopic ellipsometry (VASE), multiple-angle incidence resolution spectroscopy (MAIRS), near-edge X-ray absorption fine structure (NEXAFS) spectroscopy, sum-frequency generation (SFG) spectroscopy, and scanning tunneling microscopy (STM). In our previous work, we experimentally determined molecular orientations of 2PACz, MeO-2PACz, 3PATAT-C3, and 3CATAT-C3 on ITO using UPS and MAES[15,33,42]. In this work, we systematically applied the same procedure to Me-2PACz and Me-4PACz. The detailed analysis procedure is described in Ref. 21.

Figures 2a and 2b show the UPS and MAES spectra of Me-2PACz and Me-4PACz. Peak positions were identified from the second derivatives of the spectra. The UPS and MAES peak structures of Me-2PACz differ in both the 5.0–9.5 eV and 9.5–15 eV regions, which are associated with π orbitals and σ orbitals, respectively. The peak structures associated with π orbitals are more pronounced in UPS, whereas those associated with σ orbitals are more pronounced in MAES. A similar trend is observed for Me-4PACz. To

assign the spectral peaks to specific molecular orbitals, we performed density functional theory (DFT) calculations using the B3LYP functional and the 6-31G(d) basis set. The lower panels of Figure 2a and 2b show spectra simulated by broadening the calculated orbitals with Gaussian functions (FWHM of 0.53 eV). The calculated total density of states (DOS) was shifted in energy to align its peaks with those in the experimental UPS spectra. Then, we classified the molecular orbitals into four types, as shown in Figure S1: the π orbitals of the carbazole backbone (denoted as π orbitals) and the σ orbitals of the carbazole backbone (σ orbitals), as well as those of the linker (linker) and anchor group (anchor). The corresponding partial DOS spectra were also calculated. Peaks were labeled in order of increasing binding energy as π_1, π_2,… for π orbitals; σ_1, σ_2,… for σ orbitals; l_1, l_2,… for the linker group; and a_1, a_2,… for the anchor group. For Me-2PACz, the peaks assigned to π_{1-4} and a_1 are more pronounced in the UPS, whereas those assigned to σ_1, l_1, σ_3, $\pi_{8,9}$, and σ_5 are more pronounced in the MAES. Looking at the molecular orbitals of σ_1, σ_3, $\pi_{8,9}$, and σ_5 (Figure S2a), these orbitals extended in the in-plane direction at the upper part of the carbazole backbone. Therefore, the pronounced MAES signals from these orbitals indicate that Me-2PACz adopt a perpendicular orientation with respect to surface. Me-4PACz exhibited a similar trend. σ_1, l_2, σ_3, $\pi_{8,9}$, and σ_6 peaks in the MAES are clearer than those of UPS and corresponding molecular orbitals are shown in Figure S2b. These results indicate that Me-4PACz adopts a perpendicular orientation similar to Me-2PACz.

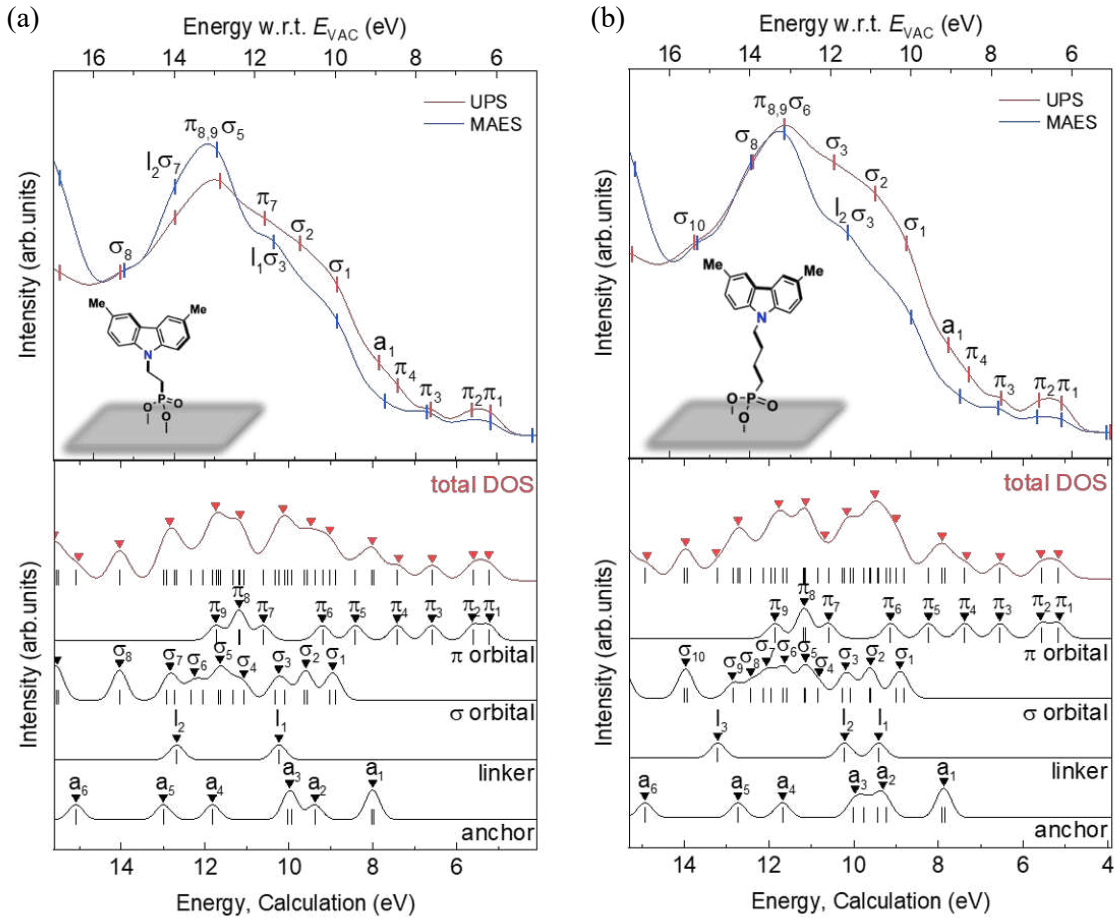


Figure 2 Experimental UPS and MAES spectra and simulated total and partial DOSs. (a) Me-2PACz and (b) Me-4PACz. The upper panels show the experimental spectra, whereas the lower panels show the simulated spectra from the calculation. Vertical bars indicate the calculated molecular orbitals, and red and black spectra show the total DOS spectra and partial DOS spectra, respectively.

We estimated the magnitude of the interface dipole using the molecular orientations and the Helmholtz equation (Eq.1). The values of $\mu_{\perp}$ were determined from the DFT-calculated dipole moments of isolated molecules, yielding 0.88 D for Me-2PACz and 0.77 D for Me-4PACz (Figure S3). N/A was assumed to be 7.12×10^{13} cm^{-2} for both molecules, based on the reported value for MeO-2PACz[15]. ε_{eff} was set to 1.9, within the reported range of 1.9–2.0[43]. The calculated the magnitude of the interface dipole were 0.12 eV for Me-2PACz and 0.11 eV for Me-4PACz. Figure 3 compares the calculated and experimental

magnitudes of the interface dipole of these two HCMs, and of 2PACz, MeO-2PACz, and 3PATAT-C3. The calculated result quantitatively reproduced the trend of the experimental values shown in Figure 1c, indicating that the magnitude of the interface dipole is predominantly determined by the permanent dipole of HCM molecules. However, the calculated values systematically underestimated the experimental values by 0.1–0.2 eV. This systematic offset can be explained by the DFT study of Sekiguchi et al., who considered 2PACz, Me-2PACz, and MeO-2PACz adsorbed on ITO[44]. Their calculations included bond dipoles at the HCM/ITO interface and structural modification of the substrate in addition to permanent molecular dipoles. The calculated values were 0.35, 0.21, and -0.05 eV for 2PACz, Me-2PACz, and MeO-2PACz, respectively, which are in good agreement with our experimental values. These findings suggest that interface bond dipoles and substrate structural modifications contribute to the underestimation obtained using the Helmholtz equation. Since these effects are almost independent of HCMs, we can reasonably evaluate the relative differences in the magnitude of the interface dipole based on the Helmholtz equation using the experimentally determined molecular orientation and dipole moments of isolated molecules obtained from DFT calculations.

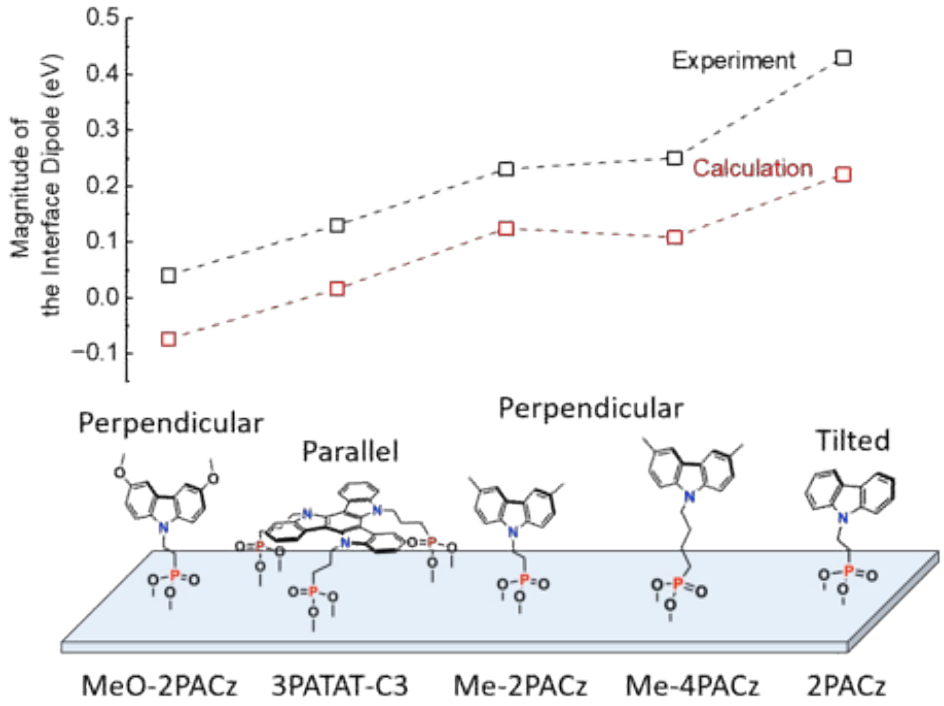


Figure 3 Calculated magnitude of the interface dipole utilizing the Helmholtz equation are compared with experimentally derived ones together with molecular orientations.

2.3. Requirement for appropriate combination of HCM and perovskite based on energy level alignment

Before exploring suitable combination of HCM and perovskite layer, we first introduce the energy level alignment model used to evaluate hole-collection efficiency. Figure 4a illustrates the energy level alignment for ITO/HCM/perovskite interfaces, which can be divided into two interfaces: the ITO/HCM (Figure 4b) and HCM/perovskite interfaces (Figure 4c). The energy level alignment at the ITO/HCM interface is described using the theory of metal/organic semiconductor interfaces[45]. As discussed above, the WF_{ITO} is modified due to the interface dipole formed by the HCM. Here, band bending within the HCM is neglected because the HCM is ultrathin (approximately 1 nm) and has a low charge density[13,46]. The

energy level alignment at the HCM/perovskite interface is described using semiconductor heterojunction theory[47]. The energy levels are aligned with respect to Fermi levels because thermal equilibrium is established upon contact between the HCM-modified ITO and the perovskite layer. This alignment results in band bending in the perovskite layer and energy barrier for hole collection. And we assume that the IE and EA of perovskite (IE_{PVK} and EA_{PVK}) remain constant throughout the perovskite layer. In this model, the hole-collection efficiency at the ITO/HCM/perovskite interface is governed by two factors: (i) band bending in the perovskite layer and (ii) the energy barrier at HCM/perovskite interface.

(i) Band bending in perovskite layer

The direction and magnitude of band bending are determined by the WF difference between HCM and perovskite (WF_{HCM} and WF_{PVK}), $\Delta WF = WF_{HCM} - WF_{PVK}$, as illustrated in Figure 4c. Figures 4d and 4e show the upward and downward band bending in the perovskite layer, respectively. When $WF_{HCM} > WF_{PVK}$ ($\Delta WF > 0$), the perovskite bands bend upward, which is favorable for hole collection. In contrast, when $WF_{HCM} < WF_{PVK}$ ($\Delta WF < 0$), they bend downward, which is unfavorable for efficient hole collection. Therefore, $\Delta WF > 0$ is required to achieve favorable upward band bending within this model.

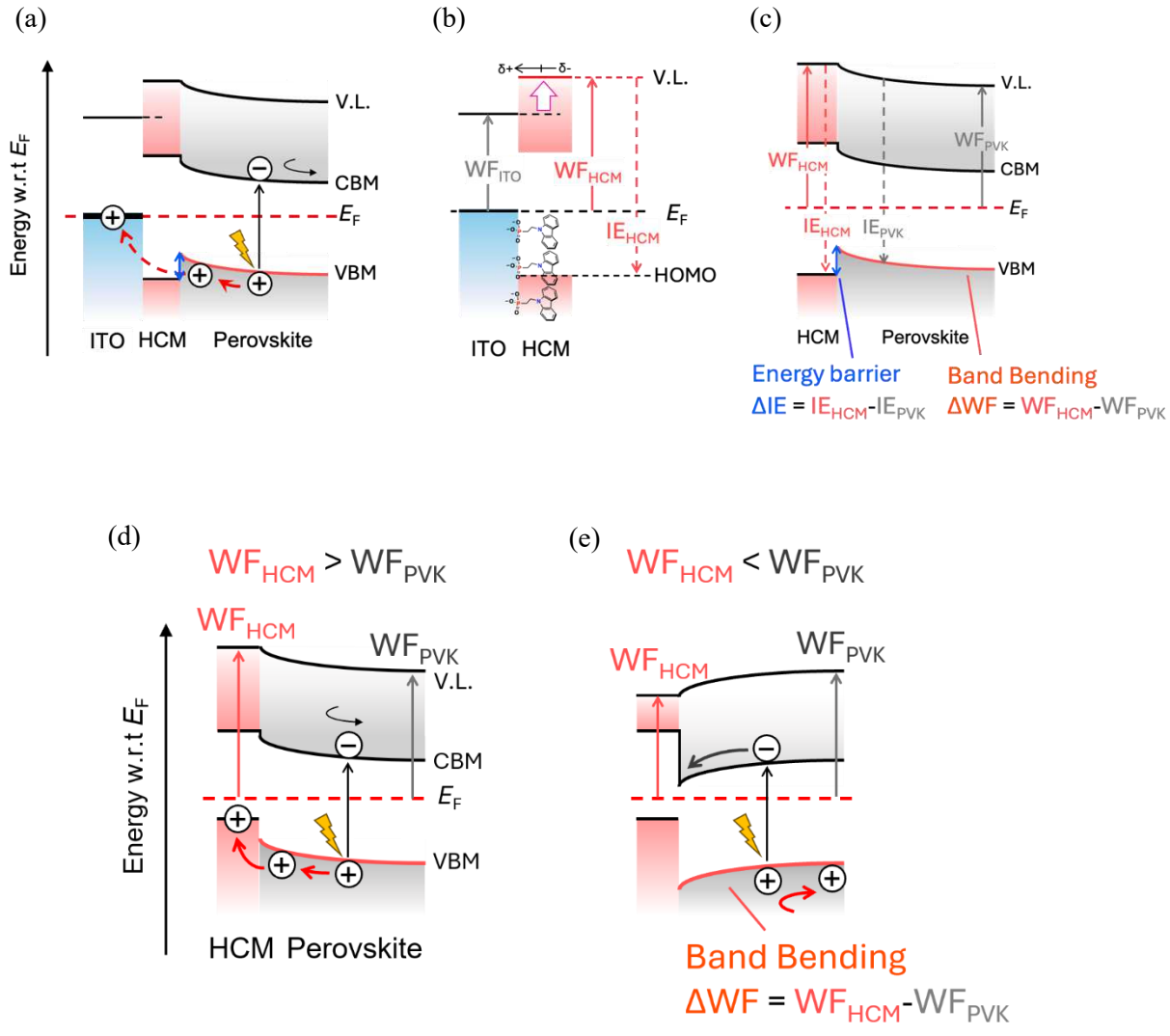
(ii) Energy barrier at HCM/perovskite interface

The energy barrier for hole collection is determined by the difference between IE_{HCM} and IE_{PVK}, $\Delta IE = IE_{HCM} - IE_{PVK}$, as illustrated in Figure 4c. Figures 4f and 4g show energy level alignments without and with an energy barrier, respectively. When $IE_{PVK} > IE_{HCM}$, i.e. $\Delta IE < 0$, no energy barrier is formed at the HCM/perovskite interface, which favors efficient hole collection. In contrast, when $IE_{PVK} < IE_{HCM}$, i.e. $\Delta IE > 0$, a barrier is formed and hinder hole collection. Therefore, the $\Delta IE < 0$ is required to efficiently collect holes from the viewpoint of energy barrier.

However, even when $\Delta IE < 0$, an excessively low IE_{HCM} may lead to V_{OC} losses. Stolterfoht et al. reported that minimizing ΔIE leads to increase V_{OC} , based on simulations and quasi-Fermi-level splitting (QFLS) measurements[48]. Thus, to achieve a high V_{OC} while maintaining efficient hole collection, IE_{HCM} should be

as close as possible to IE_{PVK} without exceeding it.

In summary, efficient hole collection requires two conditions to be satisfied simultaneously: $WF_{HCM} > WF_{PVK}$ and $IE_{PVK} > IE_{HCM}$, with ideally $IE_{PVK} \fallingdotseq IE_{HCM}$. Note that, as shown in Figure 1c, the energy difference between the Fermi level and the HOMO is similar among the HCMs. Consequently, a higher IE_{HCM} is generally accompanied by a higher WF_{HCM}, leading to larger upward band bending in the perovskite.



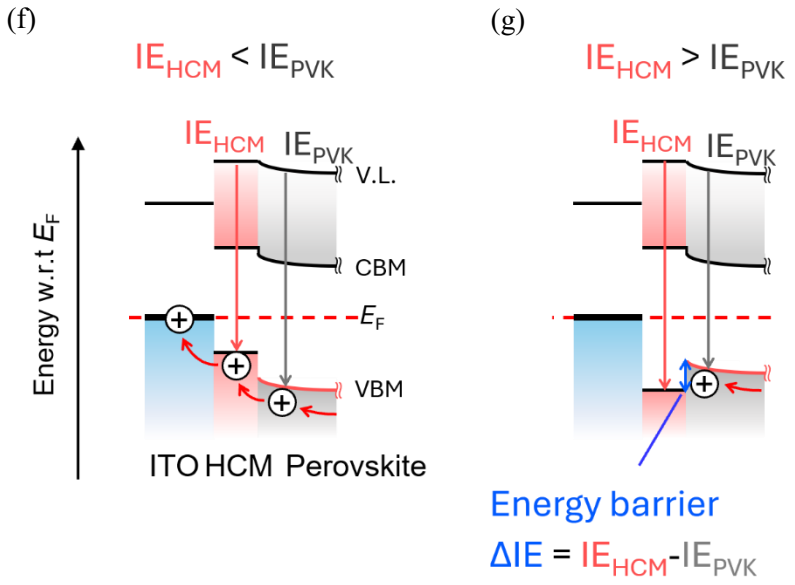


Figure 4 Energy level alignment at ITO/HCM/perovskite interfaces. (a) shows the overview of this model. (b) and (c) show energy level alignment at the ITO/HCM and HCM/perovskite interfaces, respectively. (d) and (e) represent upward and downward band bending in the perovskite layer determined by the relative values of WF_{HCM} and WF_{PVK}. (f) and (g) represent absence and presence of an energy barrier, respectively, determined by the relative values of

2.4. Appropriate combination of HCM and perovskite

Employing the energy level alignment model and the energy parameters of the HCMs and perovskites, we establish a pratical guideline for selecting an appropriate HCM for a given perovskite. The energy parameters of the HCMs were taken from Figure1c, whereas those of the perovskites were obtained from the literature. The values for single-cation perovskites were taken from Tao et al.[8] and those for double-cation perovskites ($DCPbI_{3-x}Br_x$, FA and MA denote formamidinium and methylammonium, respectively) were obtained from Prathapani et al.[35], Valerio et al.[36], and Oliver et al.[37]. For triple-cation perovskites ($TCPbI_{3-x}Br_x$), we used the values for $Cs_{0.05}FA_{0.80}MA_{0.15}PbI_{2.75}Br_{0.25}$[49] and $Cs_{0.05}FA_{0.73}MA_{0.22}PbI_{2.31}Br_{0.69}$[22]. The details are discussed in our previous work[21].

Figure 5 compares the energy parameters of the perovskites. For the WF_{PVK}, $FAPbBr_3$ exhibited the highest WF_{PVK} of 5.48 eV, whereas the WF_{PVK} decreased to 3.96 eV for $TCPbI_{2.75}Br_{0.25}$. For the IE_{PVK}, $FAPbBr_3$ exhibited the highest IE_{PVK} of 6.70 eV, whereas the IE_{PVK} decreased to 5.34 eV for $FASnI_3$. Importantly, the ordering of the perovskites by WF_{PVK} differs from that by IE_{PVK}. Therefore, the WF and IE criteria must be evaluated separately when selecting compatible HCM/perovskite combinations.

We first consider compatibility with the HCMs and perovskites in terms of band bending. Figure 5a compares the WF_{HCM} and WF_{PVK}. As discussed above, $WF_{HCM} > WF_{PVK}$ is required to induce upward band bending, which favors hole collection. Thus, all the HCMs are compatible with perovskites with WFs lower than that of $TCPbI_{2.31}Br_{0.69}$. For $FASnBr_3$, $FASnI_3$, and $CsSnBr_3$, all HCMs except MeO-2PACz satisfy $\Delta WF > 0$. Only MeO-2PACz does not satisfy this requirement due to the lowest WF of 4.79 eV, which is associated with the conformation of its methoxy group, as discussed in Ref. 21. The dipole moment can vary within -0.53–2.41 D depending on their conformation. For $FAPbI_3$, 2PACz, Me-2PACz, and Me-4PACz satisfy the band bending criterion; for $CsSnI_3$, only 2PACz and Me-4PACz satisfy it. Finally, none of the HCMs satisfy the $\Delta WF > 0$ for perovskites with WF_{PVK} higher than that of $CsPbBr_3$ because their WF_{PVK} above 5.3 eV. When the WF_{HCM} and WF_{PVK} are nearly equal, as in Me-4PACz/$CsSnI_3$ and 3PATAT-C3/$FAPbI_3$, the perovskite bands are nearly flat.

We next examine compatibility of the HCMs and perovskites in terms of energy barrier. To obtain an energy-barrier-free HCM/perovskite interface while minimizing the V_{OC} losses, $\Delta IE < 0$ is required, with IE_{HCM} as close as possible to IE_{PVK} without exceeding it as discussed above. Figure 5b compares IE_{PVK} and IE_{HCM}. The perovskites ranging from $MAPbI_3$ to $FAPbBr_3$ have sufficiently large IE_{PVK}s compared to IE_{HCM}s. Thus, any of the HCMs can be used for these perovskites without energy barrier formation. Among them, 2PACz provides the smallest ΔIE and is therefore the most favorable from the perspective of IE alignment alone. For $CsSnI_3$–$CsSnBr_3$, all HCMs except 2PACz satisfy $\Delta IE < 0$, as 2PACz has the highest IE_{HCM} (5.84 eV). Thus, Me-4PACz is the most suitable selection for these perovskites. The similar IEs of 3PATAT-C3 and Me-2PACz make them favorable choices for $DCPbI_3$–$MASnBr_3$

perovskites including $TCPbI_{2.31}Br_{0.69}$ and $TCPbI_{2.75}Br_{0.25}$. Finally, MeO-2PACz, with the lowest IE_{HCM} (5.21 eV), is preferred for compositions ranging from $DCPbI_{2.58}Br_{0.42}$ to $FASnI_3$.

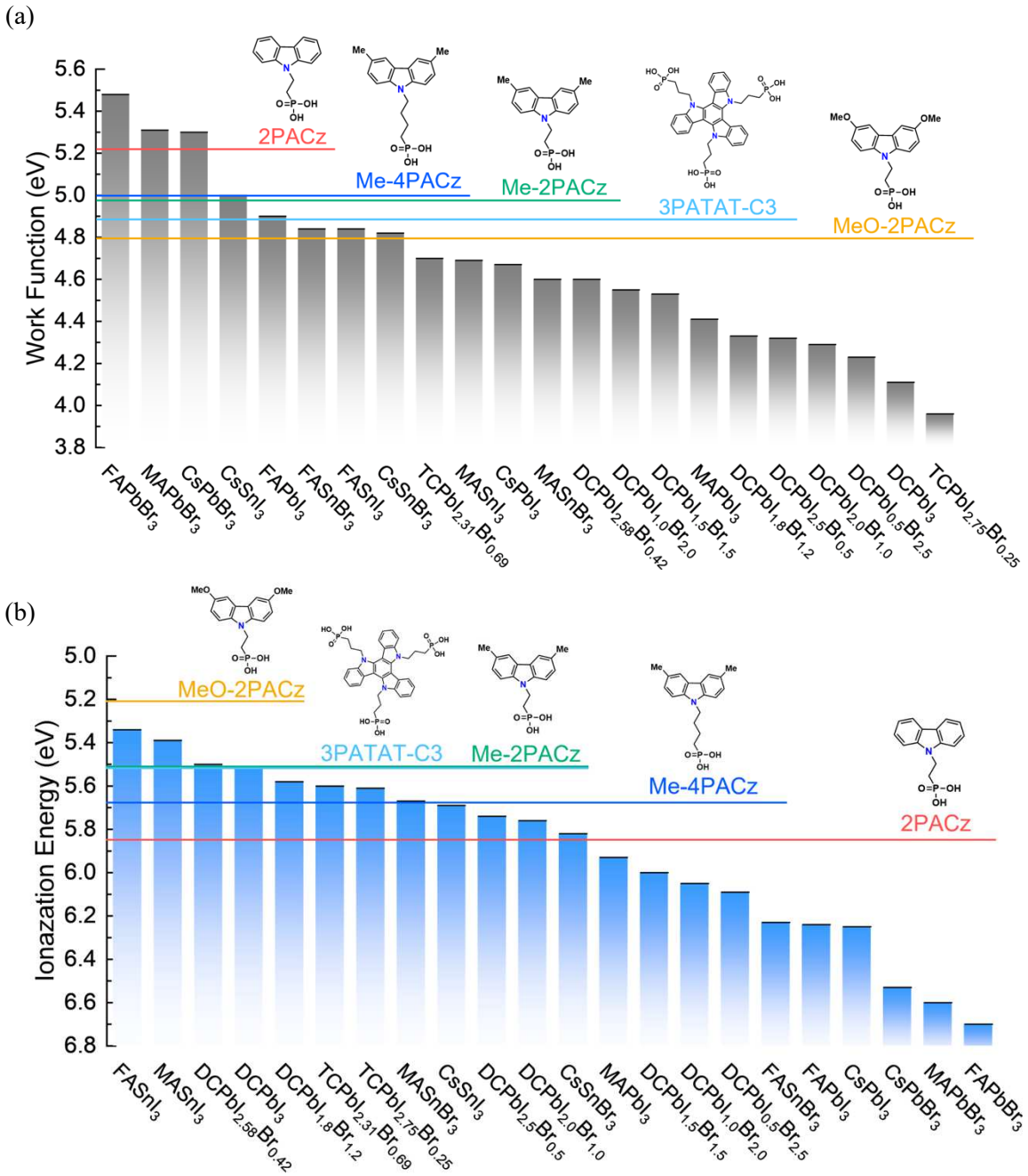
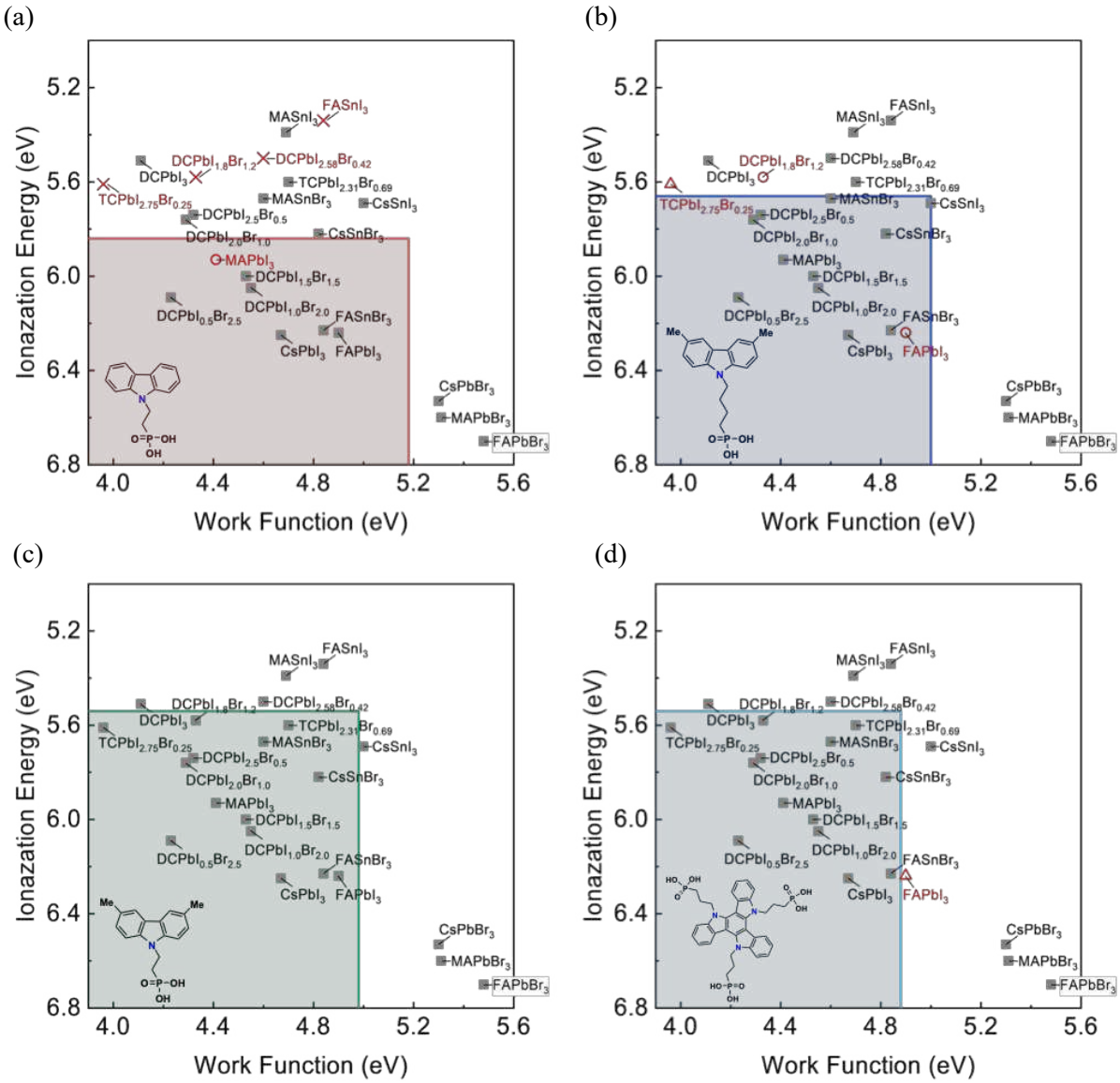


Figure 5 Comparison of energy parameters of perovskites and HCMs. (a) and (b) correspond to the work functions (WFs) and ionization energies (IEs), respectively. The bars represent the energy parameters of the perovskites, while the horizontal lines indicate those of the HCMs.

By considering both the WF and IE requirements together, we determine the optimal HCM/perovskite combinations. Figure 6 shows the WFs and IEs of various perovskites, with the colored regions indicating the ranges of WF and IE predicted to favor hole collection for each HCM. All the HCMs considered satisfy both $\Delta WF > 0$ and $\Delta IE < 0$ for $MAPbI_3$, $CsPbI_3$, $DCPbI_{0.5}Br_{2.5}$, $DCPbI_{1.0}Br_{2.0}$, and $DCPbI_{1.5}Br_{1.5}$, indicating favorable energy level alignment for these perovskites. In contrast, none of the HCMs satisfy both criteria simultaneously for $FASnI_3$, $CsPbBr_3$, $MAPbBr_3$, and $FAPbBr_3$. Thus, none of the HCMs are compatible with these perovskites.



(e)

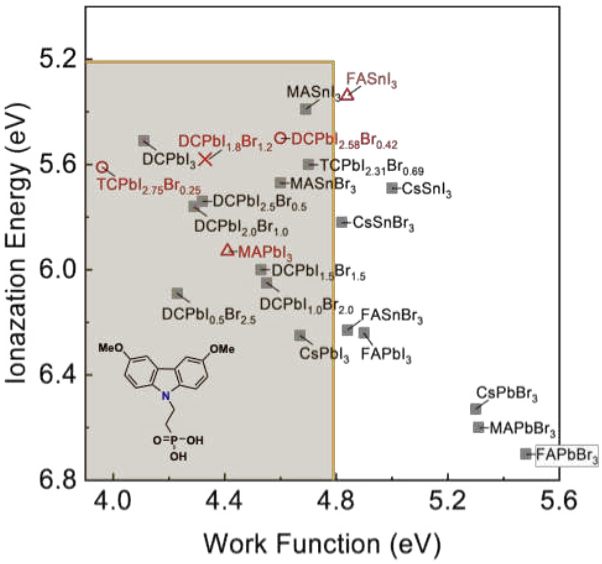


Figure 6 Energy-level compatibility between HCMs and perovskites. (a) 2PACz, (b) Me-4PACz, (c) Me-2PACz, (d) 3PATAT-C3, and (e) MeO-2PACz. The colored regions indicate the combinations of perovskite work functions (WFs) and ionization energies (IEs) predicted to be favorable for efficient hole collection by each HCM. The symbols ○, △, and × indicate relatively high, moderate, and low hole, respectively, as qualitatively assessed from reported photovoltaic parameters (V_{OC}, J_{SC}, FF, and PCE) by comparing devices employing different HCMs with the same perovskite composition. These assessments are summarized in Table S1.

We next evaluated the applicability of the HCM-selection guideline discussed above by comparing the model predictions with reported photovoltaic performance. To assess hole-collection efficiencies depending on the HCMs, we compared the reported photovoltaic parameters of devices employing different HCMs with the same perovskite composition. Based on these comparisons, we qualitatively classified the HCMs as exhibiting high (○), moderate (△), or low (×) hole-collection efficiencies for each perovskite composition. We considered the perovskite compositions for which both energy parameters and photovoltaic performance have been reported. For $DCPbI_{2.7}Br_{0.3}$, whose energy parameters were unavailable[50], we used those reported for $DCPbI_{2.58}Br_{0.42}$ because of their similar

compositions[36]. Table S1 summarizes the photovoltaic parameters (V_{OC}, J_{SC}, FF, and PCE) of devices employing different carbazole-based HCMs, together with our classification of high (◯), moderate (△), or low (×) hole-collection efficiencies. These classifications are also superimposed on the WF-IE maps in Figure 6, enabling direct comparison between the experimentally inferred relative hole-collection efficiencies and the energy-level compatibility predicted by the model.

For $MAPbI_3$, which has a low WF_{PVK} and a high IE_{PVK}, neither 2PACz nor MeO-2PACz forms an energy barrier. However, 2PACz induces stronger upward band bending (0.77 eV) and shows better photovoltaic performance than MeO-2PACz, corresponding to ○ and △ in Figure 6, respectively. A similar result is observed for $FAPbI_3$ devices employing Me-4PACz and 3PATAT-C3. Although neither combination forms an energy barrier, Me-4PACz induces stronger upward band bending and yields better photovoltaic performance (○ for Me-4PACz and △ for 3PATAT-C3). These results indicate that strong upward band bending is beneficial for hole collection when the HCM/perovskite interface is free of a hole-collection barrier. For $FASnI_3$, which has a high WF_PVK and a low IE_PVK, neither HCM satisfies both energy-level requirements: MeO-2PACz induces downward band bending ($\Delta WF < 0$), whereas 2PACz forms a hole-collection barrier ($\Delta IE > 0$). This is consistent with their poor photovoltaic performance. For $DCPbI_{2.7}Br_{0.3}$ with 2PACz or MeO-2PACz, an energy barrier is formed only with 2PACz, consistent with the better photovoltaic performance of MeO-2PACz (× for 2PACz and ○ for MeO-2PACz). For $DCPbI_{1.8}Br_{1.2}$, 2PACz forms an energy barrier, whereas MeO-2PACz induces downward band bending. In contrast, Me-4PACz induces upward band bending with almost no energy barrier and exhibits superior photovoltaic performance to the other two HCMs. This difference is indicated by ○ for Me-4PACz and × for both 2PACz and MeO-2PACz in Figure 6. Finally, $TCPbI_{2.75}Br_{0.25}$, which has low WF_{PVK} and IE_{PVK}, exhibits upward band bending with all three HCMs: 2PACz, Me-4PACz, and MeO-2PACz. The energy barrier decreases in the order 2PACz > Me-4PACz > MeO-2PACz, with MeO-2PACz yielding the best photovoltaic performance. Their hole-collection efficiencies are indicated by × for 2PACz, △ for Me-4PACz, and ○ for MeO-2PACz. Taken together,

these comparisons demonstrate that the relative hole-collection performance inferred from reported photovoltaic data can be consistently rationalized in terms of the band bending and hole-collection barriers predicted by our energy-level alignment model.

Based on the energy level alignment criteria illustrated in Figure 6, Table 1 summarizes which HCMs are suitable for each perovskite. The HCM predicted to be the most favorable based on the energy level criteria is highlighted in bold red text. The agreement between the model predicted HCM selection and reported photovoltaic performance suggests that Table 1 serve as a practical guideline for selecting HCMs expected to facilitate efficient hole collection. This guideline can also be applied to HCM/perovskite combinations that have not yet been experimentally investigated. Furthermore, the present framework can be extended to new HCMs not considered in this study, reducing the need for trial-and-error screening.

Table 1 Applicable HCMs for Each Perovskite Composition Based on Energy Level Requirements

Ref.	Perovskite Compositions	Applicable HCMs				
		2PACz	Me-4PACz	Me-2PACz	3PATAT-C3	MeO-2PACz
8	$FAPbBr_3$	–	–	–	–	–
8	$MAPbBr_3$	–	–	–	–	–
8	$CsPbBr_3$	–	–	–	–	–
8	$CsSnI_3$	–	✓	–	–	–
8	$FAPbI_3$	✓	✓	✓	–	–
8	$FASnBr_3$	✓	✓	✓	✓	–
8	$FASnI_3$	–	–	–	–	–
8	$CsSnBr_3$	–	✓	✓	✓	–
22	$TCPbI_{2.31}Br_{0.69}$	–	–	✓	✓	✓
8	$MASnI_3$	–	–	–	–	✓

8	$CsPbI_3$	✓	✓	✓	✓	✓
8	$MASnBr_3$	–	–	✓	✓	✓
36	$DCPbI_{2.58}Br_{0.42}$	–	–	–	–	✓
35	$DCPbI_{1.0}Br_{2.0}$	✓	✓	✓	✓	✓
35	$DCPbI_{1.5}Br_{1.5}$	✓	✓	✓	✓	✓
8	$MAPbI_3$	✓	✓	✓	✓	✓
37	$DCPbI_{1.8}Br_{1.2}$	–	–	✓	✓	✓
35	$DCPbI_{2.5}Br_{0.5}$	–	✓	✓	✓	✓
35	$DCPbI_{2.0}Br_{1.0}$	–	✓	✓	✓	✓
35	$DCPbI_{0.5}Br_{2.5}$	✓	✓	✓	✓	✓
35	$DCPbI_3$	–	–	✓	✓	✓
21,49	$TCPbI_{2.75}Br_{0.25}$	–	–	✓	✓	✓

✓: applicable

–:not applicable

3. Conclusion

In this study, we established a practical guideline for selecting appropriate carbazole derivative HCMs for a given perovskite with diverse compositions based on the universal energy level alignment model. We precisely determined the energy parameters of Me-2PACz and Me-4PACz on ITO by using UPS and LEIPS. In particular, we focused on the interface dipole formed by the HCM, which governs the work function of the HCM on the transparent electrode. The magnitude of the interface dipole was investigated in detail by determining the molecular orientation using UPS and MAES. This analysis revealed that both Me-2PACz and Me-4PACz adopt perpendicular orientations on ITO. Calculations based on the Helmholtz equation reproduced the experimental trend in the magnitude of the interface dipole, although an offset of approximately 0.1–0.2 eV remained between the calculated and experimental values.

We then identified appropriate HCMs for perovskites with various compositions. Based on the energy level alignment model, favorable energy level alignment for hole collection requires both $WF_{HCM} > WF_{PVK}$ and $IE_{PVK} > IE_{HCM}$, corresponding to upward band bending and the absence of an energy barrier, respectively. Using these criteria, we evaluated the compatibility with the HCMs considered with a range of perovskites. Furthermore, we assessed the prediction of its compatibility by comparing the predicted hole-collection efficiencies from the energy level alignment model with the photovoltaic performance. These results provide a practical guideline for selecting appropriate HCM/perovskite combinations and can reduce trial-and-error screening in the development of perovskite optoelectronic devices. For HCM molecules and perovskite compositions not considered in this study, their suitability can be readily evaluated using the same procedure.

Experimental

Sample preparation and Measurements

Glass/ITO substrates (Geomatec Co., Ltd.) were sequentially ultrasonicated for 15 min each in a detergent solution (Semico Clean 56, Furuuchi Chemical), water, acetone, and isopropanol. The substrates were then dried using a nitrogen gas stream and treated with UV–ozone for 20 min. The substrates were immediately transferred to an inert gas filled glove box.

Separate 1 mM solution of Me-2PACz and Me-4PACz (Tokyo Chemical Industry Co., Ltd.) in isopropanol (FUJIFILM Wako Pure Chemical Co., Ltd.) was spin-coated onto a clean ITO substrate (3000 rpm, 30s). After annealing at 100 ℃ for 10 minutes, unadsorbed Me-2PACz and Me-4PACz molecules on ITO were washed off with acetone once, and the substrates were annealed again at 100 ℃ for 1 minute. The samples were transferred into a vacuum chamber (base pressure: 3.2×10^{-8} Pa) without exposure to air for electron spectroscopy measurements.

For ultraviolet photoelectron spectroscopy (UPS) measurement, He Iα radiation (photon energy of 21.22 eV) from a He discharge lamp (SPECS, UVS 10/35) was used to measure the work function, ionization energy, and valence band. The radiation was incident on the sample at an angle of 45 °, and photoelectrons emitted normal to the samples were analyzed by an electron energy analyzer (SPECS, PHOIBOS 100). Work functions were determined from the secondary electron cutoff measured by applying a -5 V sample bias. Valence band spectra were measured without the bias voltage.

For metastable atom electron spectroscopy (MAES), metastable helium atoms (He*, excitation energy: 19.82 eV) were used as the excitation source. Singlet helium atoms (excitation energy: 20.62 eV) were removed using a quenching ramp. Measurements were performed with a He* incidence angle of 0° and an electron detection angle of 60°. A −1 V sample bias was applied, and the pressure during measurement was 5.0×10^{-7} Pa. Peak positions in the UPS and MAES spectra were determined from minima in the second

derivatives of the spectra after four times smoothing operations using a quadratic Savitzky–Golay filter with a 50-point window.

Low-energy inverse photoelectron spectroscopy (LEIPS) was performed to determine the electron affinity. Details of the LEIPS setup and measurement procedures have been described elsewhere[32,33]. A Cs–Te photomultiplier tube (Hamamatsu Photonics, R821) was used to avoid electron-excited fluorescence. A band-pass filter with a center wavelength of 285 nm was used. The vacuum level was determined from the peak position in the first derivative of the low-energy electron transmission (LEET) spectrum. The electron affinity was determined from the onset of the LEIPS spectrum relative to the vacuum level.

Author Contributions

A.A. and K. S. prepared the samples, performed the MAES, UPS, and LEIPS measurements, analyzed the data, including theoretical calculations. A.A prepared the original manuscript draft. H.Y. supervised the project. A.A. developed the model with assistance from K.S. and H.Y. All three authors jointly revised and finalized the manuscript.

Acknowledgements

This work was supported by JSPS-KAKENHI through a Grant-in-Aid for Scientific Research (A) (JP24H00446) and a Grant-in-Aid for Transformative Research Areas (A) (JP23H03939). A. A. thanks a Grant-in-Aid for JSPS Fellows (JP25KJ0718). The authors acknowledge the use of ChatGPT-5.6 Sol (OpenAI) for language editing and grammar correction.

Reference

(1) Best Research-Cell Efficiencies. https://www.nlr.gov/pv/cell-efficiency

(2) Dou, L.; Yang, Y. (Micheal); You, J.; Hong, Z.; Chang, W.-H.; Li, G.; Yang, Y. Solution-Processed Hybrid Perovskite Photodetectors with High Detectivity. *Nat. Commun.* **2014**, *5* (1), 5404. https://doi.org/10.1038/ncomms6404

(3) Nie, W.; Tsai, H.; Asadpour, R.; Blancon, J.-C.; Neukirch, A. J.; Gupta, G.; Crochet, J. J.; Chhowalla, M.; Tretiak, S.; Alam, M. A.; Wang, H.-L.; Mohite, A. D. High-Efficiency Solution-Processed Perovskite Solar Cells with Millimeter-Scale Grains. *Science* **2015**, *347* (6221), 522–525. https://doi.org/10.1126/science.aaa0472

(4) De Wolf, S.; Holovsky, J.; Moon, S.-J.; Löper, P.; Niesen, B.; Ledinsky, M.; Haug, F.-J.; Yum, J.-H.; Ballif, C. Organometallic Halide Perovskites: Sharp Optical Absorption Edge and Its Relation to Photovoltaic Performance. *J. Phys. Chem. Lett.* **2014**, *5* (6), 1035–1039. https://doi.org/10.1021/jz500279b

(5) Stranks, S. D.; Eperon, G. E.; Grancini, G.; Menelaou, C.; Alcocer, M. J. P.; Leijtens, T.; Herz, L. M.; Petrozza, A.; Snaith, H. J. Electron-Hole Diffusion Lengths Exceeding 1 Micrometer in an Organometal Trihalide Perovskite Absorber. *Science* **2013**, *342* (6156), 341–344. https://doi.org/10.1126/science.1243982

(6) Ni, Z.; Bao, C.; Liu, Y.; Jiang, Q.; Wu, W.-Q.; Chen, S.; Dai, X.; Chen, B.; Hartweg, B.; Yu, Z.; Holman, Z.; Huang, J. Resolving Spatial and Energetic Distributions of Trap States in Metal Halide Perovskite Solar Cells. *Science* **2020**, *367* (6484), 1352–1358. https://doi.org/10.1126/science.aba0893

(7) McMeekin, D. P.; Sadoughi, G.; Rehman, W.; Eperon, G. E.; Saliba, M.; Hörantner, M. T.; Haghighirad, A.; Sakai, N.; Korte, L.; Rech, B.; Johnston, M. B.; Herz, L. M.; Snaith, H. J. A Mixed-Cation Lead Mixed-Halide Perovskite Absorber for Tandem Solar Cells. *Science* **2016**, *351* (6269), 151–155. https://doi.org/10.1126/science.aad5845

(8) Tao, S.; Schmidt, I.; Brocks, G.; Jiang, J.; Tranca, I.; Meerholz, K.; Olthof, S. Absolute Energy Level Positions in Tin- and Lead-Based Halide Perovskites. *Nat. Commun.* **2019**, *10* (1), 2560. https://doi.org/10.1038/s41467-019-10468-7

(9) Kim, H.-S.; Lee, C.-R.; Im, J.-H.; Lee, K.-B.; Moehl, T.; Marchioro, A.; Moon, S.-J.; Humphry-Baker, R.; Yum, J.-H.; Moser, J. E.; Grätzel, M.; Park, N.-G. Lead Iodide Perovskite Sensitized All-Solid-State Submicron Thin Film Mesoscopic Solar Cell with Efficiency Exceeding 9%. *Sci. Rep.* **2012**, *2* (1), 591. https://doi.org/10.1038/srep00591

(10) Lee, M. M.; Teuscher, J.; Miyasaka, T.; Murakami, T. N.; Snaith, H. J. Efficient Hybrid Solar Cells Based on Meso-Superstructured Organometal Halide Perovskites. *Science* **2012**, *338* (6107), 643–647. https://doi.org/10.1126/science.1228604

(11) Zhang, H.; Park, N.-G. Progress and Issues in P-i-n Type Perovskite Solar Cells. *DeCarbon* **2024**, *3*, 100025. https://doi.org/10.1016/j.decarb.2023.100025

(12) Zhang, T.; Wang, F.; Kim, H.-B.; Choi, I.-W.; Wang, C.; Cho, E.; Konefal, R.; Puttisong, Y.;

Terado, K.; Kobera, L.; Chen, M.; Yang, M.; Bai, S.; Yang, B.; Suo, J.; Yang, S.-C.; Liu, X.; Fu, F.; Yoshida, H.; Chen, W. M.; Brus, J.; Coropceanu, V.; Hagfeldt, A.; Brédas, J.-L.; Fahlman, M.; Kim, D. S.; Hu, Z.; Gao, F. Ion-Modulated Radical Doping of Spiro-OMeTAD for More Efficient and Stable Perovskite Solar Cells. *Science* **2022**, *377* (6605), 495–501. https://doi.org/10.1126/science.abo2757

(13) Magomedov, A.; Al-Ashouri, A.; Kasparavičius, E.; Strazdaite, S.; Niaura, G.; Jošt, M.; Malinauskas, T.; Albrecht, S.; Getautis, V. Self-Assembled Hole Transporting Monolayer for Highly Efficient Perovskite Solar Cells. *Adv. Energy Mater.* **2018**, *8* (32), 1801892. https://doi.org/10.1002/aenm.201801892

(14) Pitaro, M.; Alonso, J. E. S.; Di Mario, L.; Romero, D. G.; Tran, K.; Kardula, J.; Zaharia, T.; Johansson, M. B.; Johansson, E. M. J.; Chiechi, R. C.; Loi, M. A. Tuning the Surface Energy of Hole Transport Layers Based on Carbazole Self-Assembled Monolayers for Highly Efficient Sn/Pb Perovskite Solar Cells. *Adv. Funct. Mater.* **2024**, *34* (50), 2306571. https://doi.org/10.1002/adfm.202306571

(15) Truong, M. A.; Funasaki, T.; Ueberricke, L.; Nojo, W.; Murdey, R.; Yamada, T.; Hu, S.; Akatsuka, A.; Sekiguchi, N.; Hira, S.; Xie, L.; Nakamura, T.; Shioya, N.; Kan, D.; Tsuji, Y.; Iikubo, S.; Yoshida, H.; Shimakawa, Y.; Hasegawa, T.; Kanemitsu, Y.; Suzuki, T.; Wakamiya, A. Tripodal Triazatruxene Derivative as a Face-On Oriented Hole-Collecting Monolayer for Efficient and Stable Inverted Perovskite Solar Cells. *J. Am. Chem. Soc.* **2023**, *145* (13), 7528–7539. https://doi.org/10.1021/jacs.3c00805

(16) Qu, G.; Cai, S.; Qiao, Y.; Wang, D.; Gong, S.; Khan, D.; Wang, Y.; Jiang, K.; Chen, Q.; Zhang, L.; Wang, Y.-G.; Chen, X.; Jen, A. K.-Y.; Xu, Z.-X. Conjugated Linker-Boosted Self-Assembled Monolayer Molecule for Inverted Perovskite Solar Cells. *Joule* **2024**, *8* (7), 2123–2134. https://doi.org/10.1016/j.joule.2024.05.005

(17) Liu, M.; Li, M.; Li, Y.; An, Y.; Yao, Z.; Fan, B.; Qi, F.; Liu, K.; Yip, H.-L.; Lin, F. R.; Jen, A. K.-Y. Defect-Passivating and Stable Benzothiophene-Based Self-Assembled Monolayer for High-Performance Inverted Perovskite Solar Cells. *Adv. Energy Mater.* **2024**, *14* (12), 2303742. https://doi.org/10.1002/aenm.202303742

(18) He, R.; Wang, W.; Yi, Z.; Lang, F.; Chen, C.; Luo, J.; Zhu, J.; Thiesbrummel, J.; Shah, S.; Wei, K.; Luo, Y.; Wang, C.; Lai, H.; Huang, H.; Zhou, J.; Zou, B.; Yin, X.; Ren, S.; Hao, X.; Wu, L.; Zhang, J.; Zhang, J.; Stolterfoht, M.; Fu, F.; Tang, W.; Zhao, D. Improving Interface Quality for 1-Cm2 All-Perovskite Tandem Solar Cells. *Nature* **2023**, *618* (7963), 80–86. https://doi.org/10.1038/s41586-023-05992-y

(19) Liao, Q.; Wang, Y.; Zhang, Z.; Yang, K.; Shi, Y.; Feng, K.; Li, B.; Huang, J.; Gao, P.; Guo, X. Self-Assembled Donor-Acceptor Hole Contacts for Inverted Perovskite Solar Cells with an Efficiency Approaching 22%: The Impact of Anchoring Groups. *J. Energy Chem.* **2022**, *68*, 87–95. https://doi.org/10.1016/j.jechem.2021.11.001

(20) Wu, J.; Yan, P.; Yang, D.; Guan, H.; Yang, S.; Cao, X.; Liao, X.; Ding, P.; Sun, H.; Ge, Z.

Bisphosphonate-Anchored Self-Assembled Molecules with Larger Dipole Moments for Efficient Inverted Perovskite Solar Cells with Excellent Stability. *Adv. Mater.* **2024**, *36* (28), 2401537. https://doi.org/10.1002/adma.202401537

(21) Akatsuka, A.; Truong, M. A.; Wakamiya, A.; Kapil, G.; Hayase, S.; Yoshida, H. A Universal Model for Energy Level Alignment at Interfaces of Hole-Collecting Monolayers in p-i-n Perovskite Solar Cells. *J. Mater. Chem. A* **2026**, *14* (27), 17569–17584. https://doi.org/10.1039/d5ta04749h

(22) Al-Ashouri, A.; Magomedov, A.; Roß, M.; Jošt, M.; Talaikis, M.; Chistiakova, G.; Bertram, T.; Márquez, J. A.; Köhnen, E.; Kasparavičius, E.; Levcenco, S.; Gil-Escrig, L.; Hages, C. J.; Schlatmann, R.; Rech, B.; Malinauskas, T.; Unold, T.; Kaufmann, C. A.; Korte, L.; Niaura, G.; Getautis, V.; Albrecht, S. Conformal Monolayer Contacts with Lossless Interfaces for Perovskite Single Junction and Monolithic Tandem Solar Cells. *Energy Environ. Sci.* **2019**, *12* (11), 3356–3369. https://doi.org/10.1039/c9ee02268f

(23) Ullah, A.; Park, K. H.; Lee, Y.; Park, S.; Faheem, A. B.; Nguyen, H. D.; Siddique, Y.; Lee, K.-K.; Jo, Y.; Han, C.-H.; Ahn, S.; Jeong, I.; Cho, S.; Kim, B.; Park, Y. S.; Hong, S. Versatile Hole Selective Molecules Containing a Series of Heteroatoms as Self-Assembled Monolayers for Efficient p-i-n Perovskite and Organic Solar Cells. *Adv. Funct. Mater.* **2022**, *32* (49), 2208793. https://doi.org/10.1002/adfm.202208793

(24) Tan, Q.; Li, Z.; Luo, G.; Zhang, X.; Che, B.; Chen, G.; Gao, H.; He, D.; Ma, G.; Wang, J.; Xiu, J.; Yi, H.; Chen, T.; He, Z. Inverted Perovskite Solar Cells Using Dimethylacridine-Based Dopants. *Nature* **2023**, *620* (7974), 545–551. https://doi.org/10.1038/s41586-023-06207-0

(25) Bi, H.; Liu, J.; Zhang, Z.; Wang, L.; Beresneviciute, R.; Tavgeniene, D.; Kapil, G.; Ding, C.; Baranwal, A. K.; Sahamir, S. R.; Sanehira, Y.; Segawa, H.; Grigalevicius, S.; Shen, Q.; Hayase, S. All-Perovskite Tandem Solar Cells Approach 26.5% Efficiency by Employing Wide Bandgap Lead Perovskite Solar Cells with New Monomolecular Hole Transport Layer. *ACS Energy Lett.* **2023**, *8* (9), 3852–3859. https://doi.org/10.1021/acsenergylett.3c01275

(26) Rühle, S. Tabulated Values of the Shockley–Queisser Limit for Single Junction Solar Cells. *Sol. Energy* **2016**, *130*, 139–147. https://doi.org/10.1016/j.solener.2016.02.015

(27) Eperon, G. E.; Burlakov, V. M.; Goriely, A.; Snaith, H. J. Neutral Color Semitransparent Microstructured Perovskite Solar Cells. *ACS Nano* **2014**, *8* (1), 591–598. https://doi.org/10.1021/nn4052309

(28) Eperon, G. E.; Leijtens, T.; Bush, K. A.; Prasanna, R.; Green, T.; Wang, J. T.-W.; McMeekin, D. P.; Volonakis, G.; Milot, R. L.; May, R.; Palmstrom, A.; Slotcavage, D. J.; Belisle, R. A.; Patel, J. B.; Parrott, E. S.; Sutton, R. J.; Ma, W.; Moghadam, F.; Conings, B.; Babayigit, A.; Boyen, H.-G.; Bent, S.; Giustino, F.; Herz, L. M.; Johnston, M. B.; McGehee, M. D.; Snaith, H. J. Perovskite-Perovskite Tandem Photovoltaics with Optimized Band Gaps. *Science* **2016**, *354* (6314), 861–865. https://doi.org/10.1126/science.aaf9717

(29) Yang, F.; Zhu, K. Advances in Mixed Tin-Lead Narrow-Bandgap Perovskites for Single-Junction and All-Perovskite Tandem Solar Cells. *Adv. Mater.* **2024**, *36* (31), 2314341.

https://doi.org/10.1002/adma.202314341

(30) Al-Ashouri, A.; Köhnen, E.; Li, B.; Magomedov, A.; Hempel, H.; Caprioglio, P.; Márquez, J. A.; Morales Vilches, A. B.; Kasparavicius, E.; Smith, J. A.; Phung, N.; Menzel, D.; Grischek, M.; Kegelmann, L.; Skroblin, D.; Gollwitzer, C.; Malinauskas, T.; Jošt, M.; Matič, G.; Rech, B.; Schlatmann, R.; Topič, M.; Korte, L.; Abate, A.; Stannowski, B.; Neher, D.; Stolterfoht, M.; Unold, T.; Getautis, V.; Albrecht, S. Monolithic Perovskite/Silicon Tandem Solar Cell with >29% Efficiency by Enhanced Hole Extraction. *Science* **2020**, *370* (6522), 1300–1309. https://doi.org/10.1126/science.abd4016

(31) Yoshida, H. Near-Ultraviolet Inverse Photoemission Spectroscopy Using Ultra-Low Energy Electrons. *Chem. Phys. Lett.* **2012**, *539–540*, 180–185. https://doi.org/10.1016/j.cplett.2012.04.058

(32) Yoshida, H. Principle and Application of Low Energy Inverse Photoemission Spectroscopy: A New Method for Measuring Unoccupied States of Organic Semiconductors. *Org. Electron.* **2015**, *204*, 116–124. https://doi.org/10.1016/j.elspec.2015.07.003

(33) Akatsuka, A.; Miura, M.; Kapil, G.; Hayase, S.; Yoshida, H. Direct Measurement of Electron Affinity of Carbazole-Based Self-Assembled Monolayer Used as Hole-Selective Layer in High-Efficiency Perovskite Solar Cells. *Appl. Phys. Lett.* **2024**, *124* (24), 241603. https://doi.org/10.1063/5.0215268

(34) Harada, Y.; Masuda, S.; Ozaki, H. Electron Spectroscopy Using Metastable Atoms as Probes for Solid Surfaces. *Chem. Rev.* **1997**, *97* (6), 1897–1952. https://doi.org/10.1021/cr940315v

(35) Prathapani, S.; Bhargava, P.; Mallick, S. Electronic Band Structure and Carrier Concentration of Formamidinium–Cesium Mixed Cation Lead Mixed Halide Hybrid Perovskites. *Appl. Phys. Lett.* **2018**, *112* (9), 092104. https://doi.org/10.1063/1.5016829

(36) Valerio, L.; De La Rosa, A.; Rodriguez, V.; Enriquez, C.; Telles, A.; Ramirez, Y.; Rivera, D.; Hierro, J.; Bustamante, L.; Tong, X.; Hodges, D. Characterization and Analysis of FAxCs(1−x) Pb(IyBr(1−y))3 Perovskite Solar Cells with Thickness Controlled Transport Layers for Performance Optimization. *AIP Adv.* **2019**, *9* (10), 105006. https://doi.org/10.1063/1.5123400

(37) Oliver, R. D. J.; Caprioglio, P.; Peña-Camargo, F.; Buizza, L. R. V.; Zu, F.; Ramadan, A. J.; Motti, S. G.; Mahesh, S.; McCarthy, M. M.; Warby, J. H.; Lin, Y.-H.; Koch, N.; Albrecht, S.; Herz, L. M.; Johnston, M. B.; Neher, D.; Stolterfoht, M.; Snaith, H. J. Understanding and Suppressing Non-Radiative Losses in Methylammonium-Free Wide-Bandgap Perovskite Solar Cells. *Energy Environ. Sci.* **2022**, *15* (2), 714–726. https://doi.org/10.1039/d1ee02650j

(38) Park, Y.; Choong, V.; Gao, Y.; Hsieh, B. R.; Tang, C. W. Work Function of Indium Tin Oxide Transparent Conductor Measured by Photoelectron Spectroscopy. *Appl. Phys. Lett.* **1996**, *68* (19), 2699–2701. https://doi.org/10.1063/1.116313

(39) Sugiyama, K.; Ishii, H.; Ouchi, Y.; Seki, K. Dependence of Indium–Tin–Oxide Work Function on Surface Cleaning Method as Studied by Ultraviolet and x-Ray Photoemission Spectroscopies. *J. Appl. Phys.* **2000**, *87* (1), 295–298. https://doi.org/10.1063/1.371859

(40) Wang, S.; Guo, H.; Wu, Y. Advantages and Challenges of Self-Assembled Monolayer as a Hole-

Selective Contact for Perovskite Solar Cells. *Mater. Futur.* **2023**, *2* (1), 012105. https://doi.org/10.1088/2752-5724/acbb5a

(41) Caprioglio, P.; Stolterfoht, M.; Wolff, C. M.; Unold, T.; Rech, B.; Albrecht, S.; Neher, D. On the Relation between the Open-Circuit Voltage and Quasi-Fermi Level Splitting in Efficient Perovskite Solar Cells. *Adv. Energy Mater.* **2019**, *9* (33), 1901631. https://doi.org/10.1002/aenm.201901631

(42) Truong, M. A.; Funasaki, T.; Adachi, Y.; Hira, S.; Tan, T.; Akatsuka, A.; Yamada, T.; Iwasaki, Y.; Matsushige, Y.; Kaneko, R.; Asahara, C.; Nakamura, T.; Murdey, R.; Yoshida, H.; Kanemitsu, Y.; Wakamiya, A. Molecular Design of Hole-Collecting Materials for Co-Deposition Processed Perovskite Solar Cells: A Tripodal Triazatruxene Derivative with Carboxylic Acid Groups. *J. Am. Chem. Soc.* **2025**, *147* (3), 2797–2808. https://doi.org/10.1021/jacs.4c15857

(43) Heimel, G.; Romaner, L.; Zojer, E.; Brédas, J.-L. Toward Control of the Metal−Organic Interfacial Electronic Structure in Molecular Electronics: A First-Principles Study on Self-Assembled Monolayers of π-Conjugated Molecules on Noble Metals. *Nano Lett.* **2007**, *7* (4), 932–940. https://doi.org/10.1021/nl0629106

(44) Sekiguchi, N.; Tsuji, Y.; Truong, M. A.; Wakamiya, A.; Iikubo, S. Optimization of Band Alignment by Organic Molecules for Perovskite Solar Cells. *J. Phys. Chem. C* **2025**, *129* (18), 8500–8508. https://doi.org/10.1021/acs.jpcc.4c08776

(45) Ishii, H.; Sugiyama, K.; Ito, E.; Seki, K. Energy Level Alignment and Interfacial Electronic Structures at Organic/Metal and Organic/Organic Interfaces. *Adv. Mater.* **1999**, *11* (8), 605–625. https://doi.org/10.1002/(SICI)1521-4095(199906)11:8%3C605::AID-ADMA605%3E3.0.CO;2-Q

(46) Hayashi, N.; Ishii, H.; Ouchi, Y.; Seki, K. Examination of Band Bending at Buckminsterfullerene (C60)/Metal Interfaces by the Kelvin Probe Method. *J. Appl. Phys.* **2002**, *92* (7), 3784–3793. https://doi.org/10.1063/1.1504495

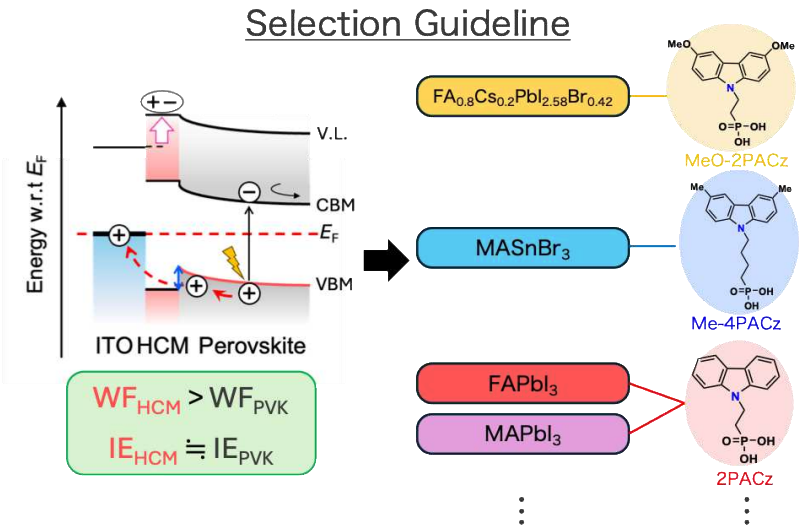
(47) P-n Junctions. In *Physics of Semiconductor Devices*; 2006; pp 77–133. https://doi.org/10.1002/9780470068328.ch2

(48) Stolterfoht, M.; Caprioglio, P.; Wolff, C. M.; Márquez, J. A.; Nordmann, J.; Zhang, S.; Rothhardt, D.; Hörmann, U.; Amir, Y.; Redinger, A.; Kegelmann, L.; Zu, F.; Albrecht, S.; Koch, N.; Kirchartz, T.; Saliba, M.; Unold, T.; Neher, D. The Impact of Energy Alignment and Interfacial Recombination on the Internal and External Open-Circuit Voltage of Perovskite Solar Cells. *Energy Environ. Sci.* **2019**, *12* (9), 2778–2788. https://doi.org/10.1039/c9ee02020a

(49) Ozaki, M.; Ishikura, Y.; Truong, M. A.; Liu, J.; Okada, I.; Tanabe, T.; Sekimoto, S.; Ohtsuki, T.; Murata, Y.; Murdey, R.; Wakamiya, A. Iodine-Rich Mixed Composition Perovskites Optimised for Tin(Iv) Oxide Transport Layers: The Influence of Halide Ion Ratio, Annealing Time, and Ambient Air Aging on Solar Cell Performance. *J. Mater. Chem. A* **2019**, *7* (28), 16947–16953. https://doi.org/10.1039/c9ta02142f

(50) Chiang, Y.-H.; Frohna, K.; Salway, H.; Abfalterer, A.; Pan, L.; Roose, B.; Anaya, M.; Stranks, S. D. Vacuum-Deposited Wide-Bandgap Perovskite for All-Perovskite Tandem Solar Cells. *ACS Energy Lett.* **2023**, *8* (6), 2728–2737. https://doi.org/10.1021/acsenergylett.3c00564

TOC Graphic



A practical guideline for selecting suitable carbazole-based hole-collecting monolayers for a range of perovskites is established using a universal energy level alignment model.

Supplementary Files

This is a list of supplementary files associated with this preprint. Click to download.

- 1026SupportingInformationver.5.2docx.docx